The Astrophysical Journal Supplement Series, 259:46 (16pp), 2022 April https://doi.org/10.3847/1538-4365/ac4d22

The First Insight-HXMT Gamma-Ray Burst Catalog: The First Four Years

Xin-Ying Song[1], Shao-Lin Xiong[1], Shuang-Nan Zhang[1,2], Cheng-Kui Li[1], Xiao-Bo Li[1], Yue Huang[1], Cristiano Guidorzi[3,4,5], Filippo Frontera[3,5], Cong-Zhan Liu[1], Xu-Fang Li[1], Gang Li[1], Jin-Yuan Liao[1], Ce Cai[1,2], Qi Luo[1,2], Shuo Xiao[1,2], Qi-Bin Yi[1,6], Yao-Guang Zheng[1,7], Deng-Ke Zhou[1,2], Jia-Cong Liu[1,2], Wang-Chen Xue[1,2], Yan-Qiu Zhang[1,2], Chao Zheng[1,2], Zhi Chang[1], Zheng-Wei Li[1], Xue-Feng Lu[1], Ai-Mei Zhang[1], Yi-Fei Zhang[1], Yong-Jie Jin[8], Ti-Pei Li[1,8], Fang-Jun Lu[1,2], Li-Ming Song[1,2], Mei Wu[1], Yu-Peng Xu[1], Xiang Ma[1], Ming-Yu Ge[1], Shu-Mei Jia[1], Bing Li[1], Jian-Yin Nie[1], Ling-Jun Wang[1], Juan Zhang[1], Shi-Jie Zheng[1], Xue-Juan Yang[6], and Rong-Jia Yang[7]

[1] Key Laboratory of Particle Astrophysics, Institute of High Energy Physics, Chinese Academy of Sciences, Beijing 100049, People's Republic of China
xiongsl@ihep.ac.cn, zhangsn@ihep.ac.cn
[2] University of Chinese Academy of Sciences, Chinese Academy of Sciences, Beijing 100049, People's Republic of China
[3] Department of Physics and Earth Science, University of Ferrara, Via Saragat 1, I-44122 Ferrara, Italy
[4] INFN—Sezione di Ferrara, Via Saragat 1, I-44122 Ferrara, Italy
[5] INAF—Osservatorio di Astrofisica e Scienza dello Spazio di Bologna, Via Piero Gobetti 101, I-40129 Bologna, Italy
[6] Department of Physics, Xiangtan University, Xiangtan, Hunan Province 411105, People's Republic of China
[7] College of Physics Sciences & Technology, Hebei University, No. 180 Wusi Dong Road, Lian Chi District, Baoding City, Hebei Province 071002, People's Republic of China
[8] Department of Engineering Physics, Tsinghua University, Beijing 100084, People's Republic of China
Received 2021 September 25; revised 2022 January 4; accepted 2022 January 10; published 2022 March 25

Abstract

The Hard X-ray Modulation Telescope (Insight-HXMT) is China's first X-ray astronomy satellite. It was launched on 2017 June 15. The anticoincidence CsI detectors of the High Energy X-ray telescope (HE) on board Insight-HXMT could serve as an all-sky gamma-ray monitor in about 0.2–3 MeV. In its first four years of operation, Insight-HXMT has detected 322 gamma-ray bursts (GRBs) by the offline search pipeline, including blind search and targeted search. For the GOLDEN sample of Insight-HXMT GRBs, joint analyses were performed with other GRB missions, including the Fermi Gamma-ray Burst Monitor (Fermi/GBM), the Swift Burst Alert Telescope (Swift/BAT), and the Gravitational wave high-energy Electromagnetic Counterpart All-sky Monitor (GECAM). The analyses showed that Insight-HXMT can provide a better constraint on the GRB spectrum at a higher-energy band. The properties of Insight-HXMT GRBs are reported in detail, including their trigger time, duration, spectral parameters, peak fluxes of different timescales, and fluence. This catalog is an official product of the Insight-HXMT GRB team.

Unified Astronomy Thesaurus concepts: Gamma-ray bursts (629)

Supporting material: machine-readable tables

1. Introduction

The Hard X-ray Modulation Telescope (HXMT), dubbed Insight-HXMT, was launched on 2017 June 15 and is China's first X-ray astronomy satellite devoted to broadband observations in the 1–250 keV band. Insight-HXMT consists of three collimator-based telescopes: the High Energy X-ray Telescope (HE; Liu et al. 2020), the Medium Energy X-ray Telescope (ME; Cao et al. 2020), and the Low Energy X-ray Telescope (LE; Chen et al. 2020). Insight-HXMT/HE adopts an array of 18 NaI(Tl)/CsI(Na) phoswich detectors as the main detector plane, with a total geometric area of about 5100 cm^2 and a combined field of view (FOV) of about $5.7° \times 5.7°$ (FWHM; HE; Liu et al. 2020). The CsI(Na) (CsI for brevity) in the phoswich detector of HE can be also used as an all-sky gamma-ray monitor in 0.2–3 MeV because gamma-rays in this energy range can penetrate the spacecraft and deposit energy in the CsI detecor. Thus HE could play an important role in monitoring gamma-ray bursts (GRBs), MeV pulsars, solar flares (SFL), terrestrial gamma-ray flashes (TGFs), and other gamma-ray sources. The measured energy range (deposited energy) of CsI is about 40–800 keV in the normal-gain (NG) mode and about 200 keV–3 MeV in low-gain (LG) mode. The NG and LG modes are achieved by adjusting the high voltage of the photomultiplier tubes (PMTs) that readout the NaI(Tl)/CsI(Na) phoswich detectors.

There is neither an on board GRB trigger system nor prompt data telemetry for Insight-HXMT, thus GRBs are unveiled on the ground using two pipelines: the blind search is performed on all data acquired by the Insight-HXMT/HE CsI detector; in addition, for each GRB that is detected by other astronomical satellites or instruments (called external triggers hereafter, in contrast to the internal triggers produced by Insight-HXMT itself) reported through the Gamma-ray Coordinates Network (GCN), the targeted search pipeline would be launched to search CsI data around the trigger time of external triggers.

From 2017 June 26 to 2021 June 30, GRBs and other bursts, including TGFs and SFLs (Zhang et al. 2021), have been detected by Insight-HXMT, the gamma-ray counterparts of gravitational wave (GW) events (Li et al. 2017, 2018; Zhang et al. 2018); fast radio bursts (FRBs; Guidorzi et al. 2020) and high-energy neutrinos (HENs; e.g., Zheng et al. 2020) have been monitored as well. During the first four years of observation data, 660 bursts are found, 322 of which are classified as GRBs, 245 as TGFs, 4 as SFLs, 33 as charged particles, and 56 as unclassified. Targeted

searches were implemented for external triggers of great importance, including 41 HENs, 48 GWs, and 39 FRBs. For each GRB, the trigger time in universal time coordinates (UTC) and mission-elapsed time (MET) are recorded and the event data are selected between $T_0 - 100$s and $T_0 + 300$s in most cases, where T_0 is the trigger time from GCN or blind search. In addition, quick-analysis tools for GRBs and joint spectral fitting with other missions are developed for this catalog analysis, which are introduced in the following sections.

We start with a brief description of the HXMT/CsI detectors and calibration in Section 2 and refer to Luo et al. (2020) for a more thorough and complete description of the instrument and calibration. This is followed, in Section 3, by the burst-searching algorithm, and its up-to-date ability is introduced in detail. In Section 4, a description of the methodology used in the production of this catalog is presented, including detector selection, data types used, energy selection, background fitting, and the source selection. In Section 5, the catalog analysis and results are presented. In Section 6, the distribution of duration and hardness is discussed, and all the GRB catalog results are summarized.

2. Instrument

The HE (Liu et al. 2020) consists of the main detector (HED), the high-energy collimator (HEC), the autogain control detector (HGC), the anticoincidence shield detector (HVT), the particle monitor (HPM), the data processing and control box (HEB), and the power box (HEA). As the main detector of HE, HED is responsible for the observation of celestial sources. It consists of 18 NaI(Tl)/CsI(Na) phoswich detectors (labeled HED-0, 1 ... to 17), each with a diameter of 190 mm and a collimator made of lead and tantalum. The NaI detectors are sensitive to the hard X-rays in 20–250 keV, whereas the CsI acts as an anticoincidence detector to reduce the background of NaI. The thickness of the NaI and CsI crystals is 3.5 mm and 40 mm, respectively. HGC provides the autogain control and energy calibration for HED. HVT acts as an active shielding system to reduce the HED background caused by charged particles. HPM monitors the flux of charged particles and sends out an alert to switch off the high voltage of HED and HVT in high-flux regions to avoid potential damage to the PMTs of these detectors. An overview of all telescopes on board Insight-HXMT is shown in Figure 1.

Insight-HXMT/HE can observe the high-energy sky with two observation scenarios (Zhang et al. 2020) that can work simultaneously:

1. Collimator-based (pointed or scan) observation: using NaI/CsI detectors, HE can detect hard X-ray emission in 20–250 keV from the celestial sources within the FOV defined by the collimators. HE can perform a pointed observation of a specific source, or it can perform a scan observation of a small sky area.
2. Gamma-ray all-sky monitoring: Gamma-ray photons with an energy higher than ∼200 keV from all directions can penetrate the spacecraft and can be detected by the CsI detectors. CsI can monitor the gamma-ray all-sky, with the only exception of the region that is occulted by the Earth. This gamma-ray all-sky monitoring is an extended capability for HE and cannot be applied for the ME or LE telescopes on board Insight-HXMT.

The primary observation scenario of HE is the collimator-based observation, consisting of a pointed observation and a scan observation, both of which use the Na I as the main detector and detect sources within the FOV of the collimator in 20–250 keV. The CsI detectors mainly act as the anticoincidence and shielding to reduce the background of NaI. Due to the high thickness of the CsI(Na) crystals, high-energy (greater than about 200 keV) gamma-ray photons can penetrate the spacecraft and can be recorded by the CsI detectors, thus the GRBs that are unocculted by the Earth can be detected. For each NaI/CsI phoswich detector of HE, the event-by-event data (called EVT data hereafter) are recorded, and we can use the pulse width information in the EVT data to distinguish between NaI events and CsI events. For this paper, we only select these events recorded by CsI detectors by screening events with a pulse width greater than 75. The response and calibration of the CsI detectors is mainly described in Section 4.1.

The gain of the NaI/CsI detector is mainly controlled by the high voltage of the PMT, which converts the scintillation light produced by NaI/CsI crystals into the electric signals. To meet various observation requirements, two gain modes are designed for the HE NaI/CsI detectors: normal-gain (NG) mode, and low-gain (LG) mode. The measured energy ranges for CsI detector are listed below: the NG mode in 40–800 keV and the LG mode in 200–3000 keV (both refer to the deposited energies). NG mode is the main working mode in which the autogain control system can keep the full-energy peak of the 59.5 keV photons (emitted from a radioactive source ^{241}Am) in a fixed channel of the NaI detector. In LG mode, the high voltage of each Insight-HXMT/HE detector is reduced and the autogain control system is disabled to achieve a higher-energy range detection. As derived from the two years of observations for which Insight-HXMT has operated in orbit, the E–C relations of each Insight-HXMT/CsI detector for the NG and LG modes vary over time, so the calibration of the instrumental response is of great importance.

3. Search for Bursts

A pipeline is developed to search for GRBs in a blind search, and the coherent search method is used for a targeted search (Cai et al. 2021). The blind-search software continually monitors each group (18 CsI detectors are divided into six groups, with three detectors in each group) of detector count rates to reduce the statistical fluctuations of one or a few detectors. These fluctuations are one of the main causes of false triggers. The pipeline is triggered when count rates in the EVT data of three or more groups of CsI detectors exceed the background count rates by 3σ on five timescales: 0.05 s, 0.1 s, 0.2 s, 0.5 s, and 1 s by calculating an average of the count rates of 10 s of the previous data as background.

If a GRB that is detected by other external missions falls in the FOV of HE, but did not trigger the blind search, a targeted search in HE/CsI data is launched. The targeted coherent search method is applied to the EVT data of the HE CsI detectors, which can recover true astrophysical bursts that are too weak to trigger through a blind search. This coherent method was originally developed by Blackburn et al. (2015), was improved by Goldstein et al. (2016, 2019), and was verified by Kocevski et al. (2018). From the statistics of searched GRBs, we that find the fluence (from the GBM Burst Catalog) of HE targeted search could reach $\sim 10^{-7}$ erg cm^{-2} (10 keV–1 MeV) for a duration of 0.256 s. For this paper, 15 GRBs that were found from targeted search are included and labeled in Table 3, while the rest are from a blind search. Details of the burst search are presented in a separate paper (Cai et al. 2021).

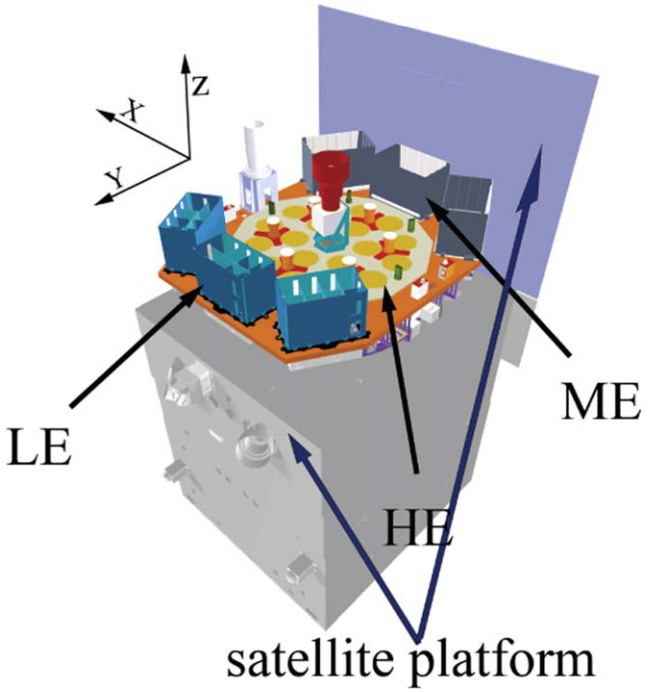

Figure 1. Illustration of the satellite platform and the payloads of Insight-HXMT. The coordinate system used in this study is shown in the upper left corner. It is adapted from Figure 1 in Luo et al. (2020).

4. Catalog Analysis

4.1. Instrument Response

There are two parts in the instrumental response of CsI detectors: the energy redistribution of the photons from incident energy to deposition energy that is determined by the property of the CsI crystal and the mass distribution of the satellite, and the energy–channel (E–C) relation that is determined by the detectors and by the electronic system of the instrument. For the photon energy redistribution, the reliability is mainly determined by the accuracy of the mass model of the satellite and the payloads (Agostinelli et al. 2003). Based on the initial mass model of the satellite platform (Xie et al. 2015), we calibrate the mass model with the Crab pulse radiation as a standard candle (Li et al. 2018) to generate an accurate instrumental response for the all-sky gamma-ray monitoring.

The in-flight E–C relation and energy resolution of the instrument can be obtained by analyzing the characteristic lines of the in-orbit observed and the on-ground simulated background spectra (Li et al. 2019). The E–C relation varies over time, whereas the energy resolution remains stable (Li et al. 2020). Therefore, we update the E–C relation every month, and take the average energy resolution of all calibration results to generate the instrumental response.

After the above calibration, a new response matrix library is established and a simulated spectral analysis is performed to test the HXMT/CsI spectroscopy capabilities. Calibration of the instrumental response to GRBs is carried out with GRBs (Luo et al. 2020). In a GRB observation, the incident direction of the GRB photons is supposed to be arbitrary, but only the instrumental response to several directions can be calibrated directly. A common method of the instrumental response testing is the cross-calibration with other instruments by comparing the energy spectrum of the simultaneously observed GRBs (Sakamoto et al. 2011; Tierney 2011; Tsujimoto et al. 2011; Ishida et al. 2014). The detection efficiency of HXMT/CsI is checked by the joint spectral analyses with Fermi/GBM, Swift/BAT, and Konus-Wind, in which we find that HXMT/CsI can provide a better constraint on the GRB spectrum at a higher-energy band (Luo et al. 2020). The instrumental responses are mainly obtained by Monte Carlo simulation with the Geant4 tool and the mass model of both the satellite and all the payloads, which is updated and tested with the Crab pulse emission in various incident directions. Both the E–C relation and the energy resolution are calibrated in two working modes (NG mode and LG mode) with the different detection energy ranges. The simulated spectral analyses show that HXMT/CsI can constrain the spectral parameters much better in the high-energy band than in the low-energy band. As introduced in Luo et al. (2020), the joint spectral analyses are performed for 10 bright GRBs observed simultaneously with HXMT/CsI and other instruments (Fermi/GBM, Swift/BAT, and Konus-Wind), and the results show that the GRB flux given by HXMT/CsI is systematically higher by $7.0 \pm 8.8\%$ than those given by the other instruments. The HXMT/CsI- I-Fermi/GBM joint fittings also show that the high-energy spectral parameter can be constrained much better as the HXMT/CsI data are used in the joint fittings.

In summary, the instrumental responses of the HXMT/CsI detectors of Insight-HXMT are well calibrated in aspects of mass model, E–C relation, and the energy resolutions for both the NG and LG modes. Thanks to the large effective area in the high-energy band, as shown in Figure 2, HXMT/CsI shows its advantages in constraining the GRB spectra in the high-energy band, together with other missions (such as Fermi/GBM), which provide observations at lower energies.

Note that the the deposited energy range is usually very different from the incident energy bands due to the responses of HXMT/CsI detectors. Three types of spectra are listed in Table 1, where the soft and middle spectra are with the BAND model and the hard spectra is with the CPL model, and they are representative of GRBs of different hardness; details of the BAND and CPL model are clarified in Section 4.7.1. They are simulated with the same amplitude in each type of spectra (using *fakeit* in Xspec 12.11.0, with all the model normalization factors equal to 1), and convoluted with the total response of 18 HXMT/CsI detectors. The deposited energy spectra of an incident angle theta from 0° to 180° are shown in NG mode (Figure 3) and in LG mode (Figure 4), which shows the ranges of the deposited energy. Considering the deposited spectra and effective area shown in Figure 2, the deposited energy range of HXMT/CsI data is determined to be about 150–800 keV for NG mode and about 200–3000 keV for LG mode in the following spectral analysis.

4.2. GRB Samples

In summary, we define three types of GRB samples as shown in Table 2. Only the "GOLDEN" GRBs could be used in the joint analysis. They are required to be located well and detected without saturation in HXMT/CsI data. The "SILVER" samples denote GRBs that are detected by other external missions, but are not located or lack data for a joint analysis. In this analysis, public data offered by Fermi/GBM, Swift/BAT, or GECAM are used for the joint analysis. The bursts that are only detected by HXMT are labeled "BRONZE". The HXMT/HE data files will not be used if there is saturation in the electronics subsystem during the GRBs, or if the data quality is not good (e.g., data loss). Saturation is defined when the two following criteria are matched simultaneously: first, the total

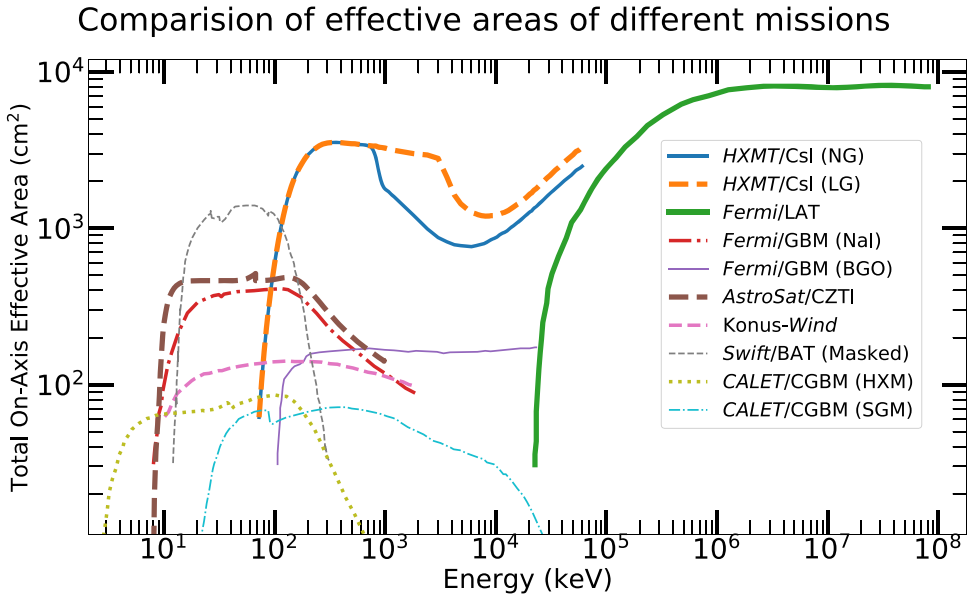

Figure 2. Effective areas of HXMT/CsI, , Fermi/LAT, Fermi/GBM, Konus-Wind, Swift/BAT, CALET/CGBM, and AstroSat/CZTI. The effective area of Fermi/GBM (NaI) is averaged over the unocculted sky. It is adapted from Figure 13 in Luo et al. (2020).

Table 1
Three Types of Spectra and Parameters

Types of Spectra	α	β	$E_{\rm peak}$ (keV)
SOFT	−1.9	−3.7	70
MIDDLE	−1.0	−2.0	230
HARD	−0.5	⋯	1500

Note. The soft and middle spectra are with the BAND model, and the hard spectrum is with the CPL model.

count rate of the 18 CsI detectors exceeds 20,000 counts s^{-1}, as evaluated over four different timescales: 0.1, 0.2, 0.5, and 1.0 s; second, in at least one of the three groups of 6 CsI detectors that share the same analog-to-digital converter (ADC; Liu et al. 2020), the total light curve has at least one 5 ms bin with zero counts. As shown in Table 2, these types of GRB samples are labeled "IRON". They are not used in the following analysis.

4.3. Suppression of Background from Charged Particles

Among the main detectors of the HE telescope, HVTs act as an active shielding system to reduce HED background caused by charged particles (HE; Liu et al. 2020). In order to suppress the background from charged particles, events that are coincident with signal in HVTs are removed because they are likely produced by charged particles rather than gamma-rays. In addition, events that also have an energy deposition in the NaI(Tl) detectors are also eliminated because the signals of NaI (Tl) are mainly from the target source when we perform a pointed or scan observation. The responses of the 18 CsI detectors in HED according to Section 2 are different, but the discrepancy between them is small (unlike for Fermi/GBM or GECAM, where the detectors have different orientations), therefore, all data events in the 18 CsI detectors are used in this study.

4.4. Dead-time Correction

The dead time of the HED detectors is complicated. According to Xiao et al. (2020), every 6 detectors in 18 NaI (Tl)/CsI (Na) detectors in HE share one ADC readout electronics, thus a signal in any detector will cause dead time not only to the incident detector itself, but also to the other 5 detectors of the same ADC. The dead time of one event is normally about 4 ∼ 8 μs, but it will be longer for signals generated by high-energy charged particles. There is a dead-time counter in HEB for each HED, and the information is recorded in the form of the proportion of dead time. The proportion of dead time in a time interval is determined with the method established in Xiao et al. (2020). The correction factors on the light curves are determined by $\frac{1}{1-P_{\rm dt}}$, where $P_{\rm dt}$ is the proportion of dead time in every time bin with a bin width of 10 ms. The light curves of each CsI detector are corrected by multiplying with a series of dead-time correction factors before background fitting is performed. In Figure 5, the comparison between light curves with and without dead-time correction of a short GRB is presented, which shows that the dead-time correction is necessary for a refined analysis.

4.5. Background Fitting

After the data have been selected for a given GRB, a background model in the form of a polynomial function with time is computed separately for each detector, based on user-selected time intervals for the background region. Here we use a preburst interval and a postburst interval as user-selected background regions. The order of the polynomial is determined by the best goodness of fit with polynomials of different orders, where the order could be 0, 1, or 2. For each detector, background fitting is carried out for each energy channel, and the background fits determined from preburst and postburst intervals are used to estimate the background counts in the signal region of the burst. The net count number of GRBs in each channel is obtained by subtracting the background counts from the total count number. Background fitting is performed in each detector channel by channel in the deposited energy spectrum, until the net counts and background counts of all channels for the given GRB are determined. Statistical errors of the net counts are determined by the root of the sum of squares of the statistical errors of the background estimation and Poisson errors of the total counts (i.e., classical error propagation). Note that all light curves for each

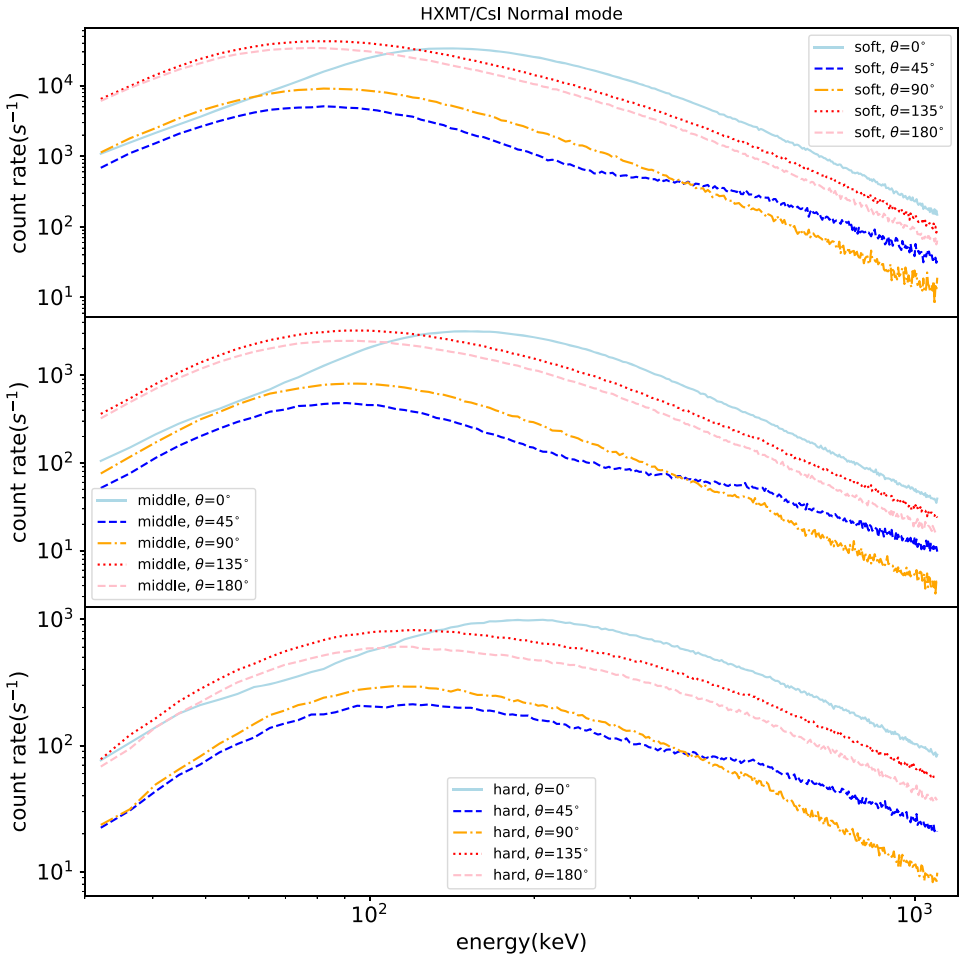

Figure 3. The deposited energy spectra of three types of BAND with an incident angle θ of 0°–180° are shown in NG mode. The azimuthal angle ϕ is 0°. Here the incident angle θ and the azimuthal angle ϕ denote the direction of gamma-rays in spherical coordinates of the HE/CsI detector.

energy channel in each detector have been corrected with dead-time correction factors. The source time intervals for all detectors are chosen to be same for the GRB data analysis, thus data of all detectors could be added up to reduce the statistical uncertainties.

4.6. Source Time Interval Selection

Source time interval selection may be different when we perform different analyses. For the computation of the duration, peak fluxes, and fluence, the source interval is loosely selected by starting from several seconds before the burst begins and ending at several seconds after the burst ends, and this may overlap with preburst and postburst intervals for the background selection. If a difference exists of the start and end time of a GRB between HXMT/CsI and other missions due to the energy detection range, the loosest source interval is applied for the joint data analysis of these missions. For the analysis of time-averaged spectra, the source time interval is usually selected to be narrower. The events in T_{90} or the whole duration in some cases based on the deposited photon counts are selected for the time-averaged energy spectra.

In the case of joint analyses with other missions, the time delay due to the different arrival times of two spacecraft is considered. The method mentioned in Hurley et al. (1999) is used to determine the time delay between HXMT and other missions. Figure 6 shows the time delays of other missions relative to HXMT for the "GOLDEN" GRB samples. The red histograms denote the time delays of Fermi/GBM, while the blue histograms denote those of Swift/BAT and the green histograms show those of GECAM. Negative values mean that GRBs arrived earlier at other missions than at HXMT, while positive numbers mean that the GRB arrival time at HXMT is earlier. Some time delays reach up to some dozen milliseconds and must be considered, because the timescale (64 ms) of the deconvolved photon spectra is on the same order of magnitude.

4.7. Duration, Fluence, and Peak Flux

In order to take advantage of the different missions and to reduce uncertainties in the determination of the parameters of GRBs, joint spectral analyses between HXMT and Fermi/GBM, Swift/BAT, and GECAM are applied on all "GOLDEN" GRBs. This paper reports various measures of the duration, peak fluxes, and fluence of each burst. We take GRB 200125B (HEB200125863), GRB 210121A (HEB2101210779), and GRB 210112A (HEB210112068) as samples to show the procedures we performed on all GRBs in the Appendix. The fits to time-averaged and time-resolved spectra are all performed with Xspec 12.11.0.

4.7.1. Time-averaged Spectrum

The time-averaged energy spectra are obtained from HXMT/CsI together with other instruments. For example, from Fermi/GBM, the spectra from two NaI(Tl) scintillation detectors working at 8 keV–1 MeV and one BGO scintillation detector at

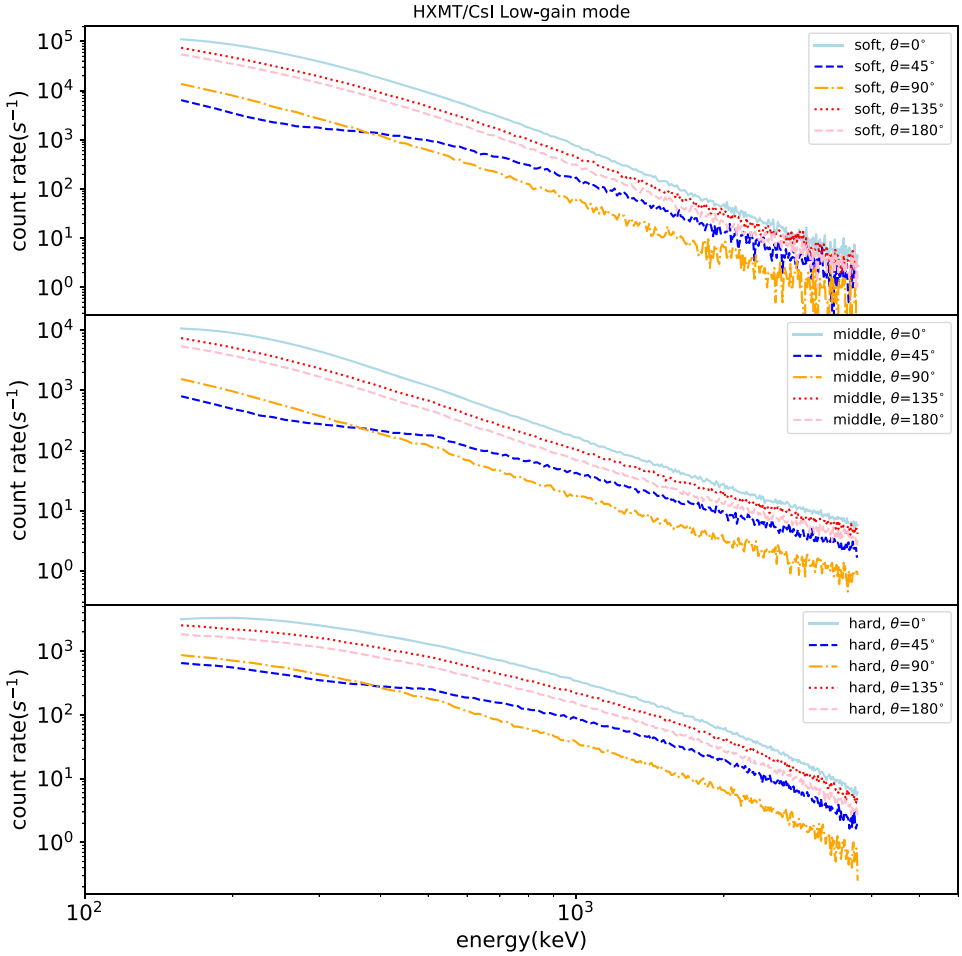

Figure 4. The deposited energy spectra of three types of BAND with an incident angle θ of 0° to 180° are shown in LG mode. The azimuthal angle ϕ is 0°. Here the incident angle θ and the azimuthal angle ϕ denote the direction of gamma-rays in spherical coordinates of the HE/CsI detector.

Table 2
Classification of Four Types of Insight-HXMT GRB Samples

Type	Location and Data for Joint Analysis	External Detected	Saturation in HXMT Data	Used or Not Used	Number
GOLDEN	Yes	Yes	No	Yes	202
SILVER	No	Yes	No	No	44
BRONZE	No	No	No	No	50
IRON	Yes/No	Yes/No	Yes	No	26

~200 keV–~4 MeV are selected according to the statistics of the GRB signal. A joint fit with time-averaged energy spectra from HXMT/CsI and three (two NaI and one BGO) spectra from Fermi/GBM is performed, where the parameters of the GRB spectral shape are shared but the amplitudes are set to be free for these four sets of data, to compensate for the possible lack of information either in the adopted spectrum model or in the understanding of the instrument response. In most cases, the amplitudes of the fitted spectra are well consistent with each other within one standard deviation.

To perform the joint fit, six models are chosen, including a single power law (PL), Band's GRB function (BAND; Band et al. 1993), an exponential cutoff power law (CPL, also called Comptonized model), and a component of the blackbody function (BB) of float amplitudes. The PL model is represented with Equation (1) with two free parameters, where A denotes the amplitude and α is the spectral index,

$$N_{\rm PL}(E) = AE^{\alpha}. \quad (1)$$

The BAND function has four free parameters: low- and high-energy spectral indices, denoted α and β, respectively, the peak energy of the νF_{ν} spectrum, denoted $E_{\rm peak}$, and the amplitude, as shown in Equation (2),

$$N_{\rm BAND}(E) = A\begin{cases}\left(\frac{E}{100\ \rm keV}\right)^{\alpha}\exp\left[-\frac{(\alpha+2)E}{E_{\rm peak}}\right], & E \geqslant \frac{(\alpha-\beta)\,E_{\rm peak}}{\alpha+2} \\ \left(\frac{E}{100\ \rm keV}\right)^{\beta}\exp(\beta-\alpha)\left[\frac{(\alpha-\beta)E_{\rm peak}}{100\ \rm keV\ (\alpha+2)}\right]^{\alpha-\beta}, & E < \frac{(\alpha-\beta)\,E_{\rm peak}}{\alpha+2}.\end{cases} \quad (2)$$

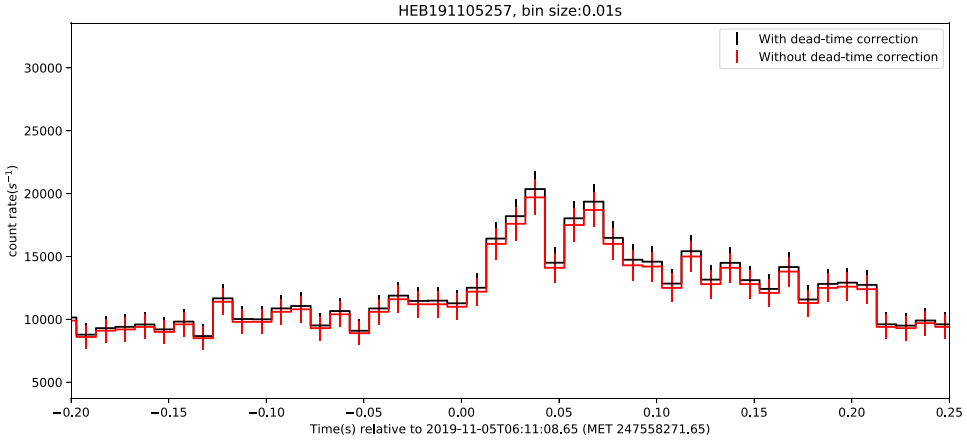

Figure 5. A comparison between light curves with and without dead-time correction of a short GRB triggered on 2019 November 05 T06:11:08.65 UTC. The histogram of red lines and the error bars denote the light curve without dead-time correction, while the black histogram shows the light curve with dead-time correction. Here MET means the mission-elapsed time of HXMT.

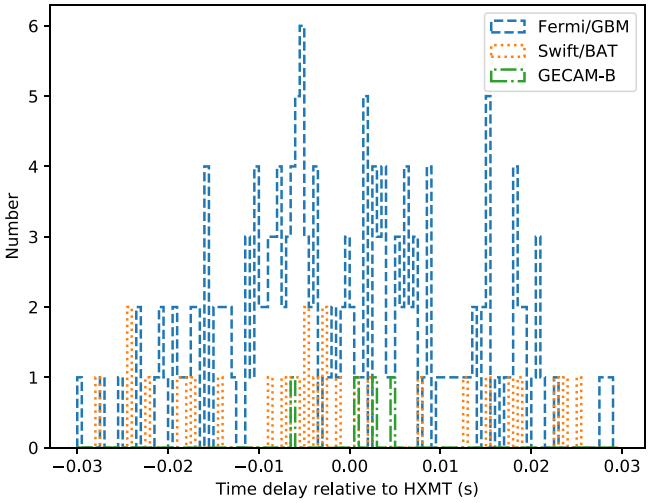

Figure 6. The distribution from the "GOLDEN" GRB samples of the time delays of Fermi/GBM (dashed), Swift/BAT (dotted), and GECAM (dot–dashed) relative to HXMT.

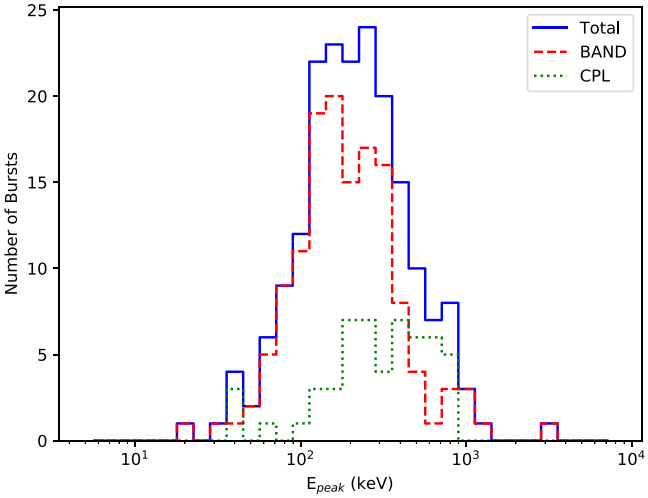

Figure 8. The distribution of the νF_ν peak energy $E_{\rm peak}$ of "GOLDEN" GRBs from time-averaged spectral fits. The solid blue lines denote the total distribution of $E_{\rm peak}$ from the BAND model (dashed red lines) and the CPL model (dotted green lines).

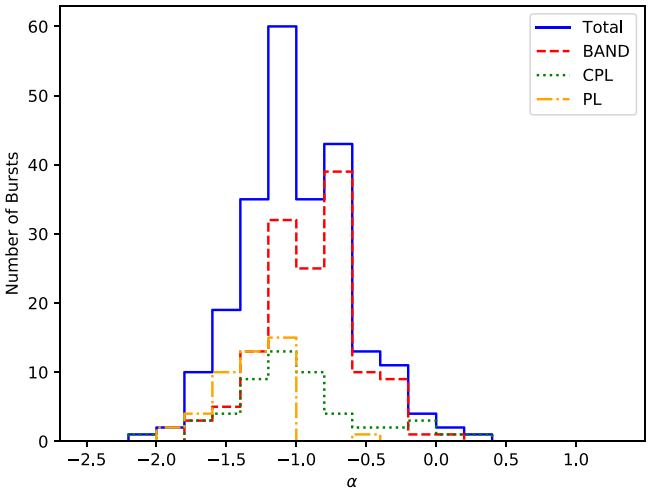

Figure 7. The distribution of the low-energy spectral index α of "GOLDEN" GRBs from time-averaged spectral fits. The solid blue lines denote the total distribution of α from the BAND model (dashed red lines), the CPL model (dotted green lines), and the PL (dotted–dashed orange lines).

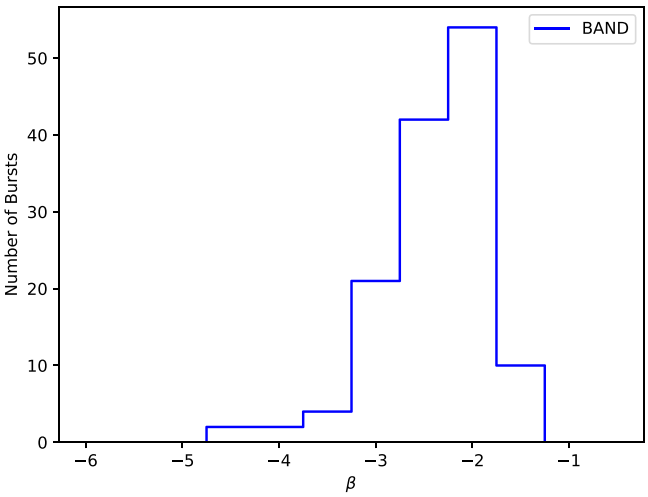

Figure 9. The distribution of the high-energy spectral index β of "GOLDEN" GRBs from time-averaged spectral fits.

The CPL model is a subset of the BAND model if β is very small and the part of $E < \frac{(\alpha-\beta)\,E_{\rm peak}}{\alpha+2}$ of the BAND model is ignored. There are three parameters in the CPL model: the amplitude A, the lower-energy index α, and the νF_ν peak energy, $E_{\rm peak}$, as shown in Equation (3),

$$N_{\rm COMP}(E) = A\left(\frac{E}{E_{\rm piv}}\right)^{\alpha}\exp\left[-\frac{(\alpha+2)\,E}{E_{\rm peak}}\right]. \quad (3)$$

Equation (4) for the photon spectrum of a blackbody is usually used in the spectral fitting, where $K = L_{39}/D^2_{\rm L,10kpc}$ is defined by the blackbody luminosity L in units of 10^{39} erg s^{-1} in the GRB host galaxy frame and the luminosity distance $D_{\rm L}$ in units of 10 kpc,

$$N_{\rm BB}(E) = \frac{K\times 8.0525E^2}{(kT)^4[\exp(E/kT)-1]}. \quad (4)$$

All models are formulated in units of photon flux with energy (E) in keV and are multiplied by a normalization constant A (ph s^{-1} cm^{-2} keV^{-1}), and kT and E are measured in the observer's frame. We determine the best spectral parameters by optimizing the Castor C statistic value. Castor Cstat (henceforth Cstat; Cash 1979) is a likelihood technique modified for a particular data set to converge to a χ^2 with an increase in signal. χ^2 is evaluated for each spectral fit that is performed through minimizing Cstat. The best of these six models is determined when a single additional parameter changes in χ^2 by at least 6 because the probability for achieving this difference is 0.01, as suggested by Goldstein et al. (2012), which is a conservative threshold to avoid the false-positive rates of the additional component.

As shown in the Appendix, for GRB 200125B (HEB200125863), a joint spectral fit with the BAND model is the best model, with a reduced χ^2 of 1.14. *A*-BAND model with a low-energy spectral index $\alpha = -0.78 \pm 0.01$, a high-energy spectral index $\beta = -2.70 \pm 0.03$, and the νF_ν peak energy, $E_{\rm peak} = 200.8 \pm 7.7$ keV, is determined. GRB 210121A is observed by HXMT/CsI, Fermi/GBM, and GECAM, and the joint analysis is performed with the other two missions. $\alpha = -0.64 \pm 0.01$, $\beta = -2.49 \pm 0.03$, and $E_{\rm peak} = 932.4 \pm 23.8$ keV are determined with the BAND model. GRB 210112A is detected by Swift/BAT and HXMT/CsI. The best model is determined to be CPL, with $\alpha = -1.27 \pm 0.03$ and $E_{\rm peak} = 347.7 \pm 49.7$ keV for the CPL component. When only data of Swift/BAT are used, the PL model is determined and $E_{\rm peak}$ is not measured due to lack of information from the higher-energy band.

The distribution of the energy spectrum parameters of "GOLDEN" GRBs is shown in Figures 7–9. Up to 29% low-energy spectral indices of the "GOLDEN" samples violate the $-2/3$ synchrotron line of death (Preece et al. 1998), while an additional 6% of the indices violate the $-3/2$ synchrotron cooling limit. The distribution of high-energy indices in Figure 9 peaks at a slope slightly steeper than -2 and has a extension toward steeper values. The $E_{\rm peak}$ distribution generally peaks around 200 keV and spans over two orders of magnitude.

4.7.2. Duration and Fluence

For the "SILVER" and "BRONZE" samples, the burst durations are determined by integrating the signal counts from GRBs with a deposited energy in ranges of 40–800 keV in NG mode and 200–3000 keV in LG mode, respectively. The durations T_{50} and T_{90} are determined from the interval between the times where the burst has reached 25% (5%) and 75% (95%) of its maximum counts. The method developed for BATSE (Koshut et al. 1996) is used to determine the systematic error. Table 5 shows the duration values of the "SILVER" and "BRONZE" samples.

For the "GOLDEN" samples, the burst durations T_{50} and T_{90} are computed in the 10–2000 keV energy range. They are determined using a method similar to that developed for BATSE (Koshut et al. 1996), the count spectra of HXMT/CsI and the other missions in each time bin of 64 ms are deconvolved and the durations are computed from the time history of the fitted photon spectra. Peak fluxes of different timescales are naturally obtained in the same analysis, and the fluence is obtained by integrating the deconvolved flux history.

It is worth noting that to avoid the failure of the fit to each time bin, the parameters of the GRB shape are fixed to the best model determined in a joint fit to the time-averaged spectrum, while the amplitudes are set to be free. Therefore, in addition to the systematic effects mentioned in Koshut et al. (1996), an additional systematic error is introduced by the fixed parameters. To estimate the uncertainty from the fixed parameters, we simulate tens of sets of parameters of the best GRB model by smearing the mean values with a covariance matrix within one standard deviation. Then the same procedures are applied to calculate tens of sets of duration values. The maximum changes from the duration values with the mean value are taken to be the systematic error from fixed GRB parameters. The systematic uncertainties of the peak fluxes and fluences from the same source are also estimated in the same way. Note that in most cases of the spectral parameters that are well determined, the system uncertainties of this type are smaller than or numerically comparable with the systematic effects, which can be ignored. As a sample of GRB 200125B, the total fluence (10–2000 keV) is $5.92 \times 10^{-5} \pm 4.54 \times 10^{-7}$ erg cm^{-2}, and the peak flux (ph cm^{-2} s^{-1}) in 10–2000 keV on timescales of 64 ms, 256 ms, and 1024 ms is 175.35 ± 9.57, 149.25 ± 3.78, and 110.27 ± 1.63 respectively.

5. Catalog Results

Table 3 lists the 322 searched bursts that are classified as GRBs. In the last column of Table 3, abbreviations of GRB types are given. Out of 322 searched bursts files, 202 "GOLDEN" samples are analyzed and collected in total. Forty-four "SILVER", 50 "BRONZE", and 26 "IRON" samples are also listed in Table 2.

The results of the duration of the GRBs are derived from joint analyses of HXMT with Fermi/GBM, Swift/BAT, or GECAM as discussed in Section 4.7 and shown in Table 4. The values of T_{50} and T_{90} in the 10–2000 keV energy range are listed along with their respective statistical error estimates and start times relative to the trigger time of HXMT. As part of the duration analysis, peak fluxes and fluence are computed. Table 5 lists the durations of the "SILVER" and "GOLDEN" samples, which were obtained from HXMT/CsI GRB signal counts. Table 6 shows the total fluence and peak fluxes of different timescales in 10–2000 keV.

Table 3
GRB Triggers: Locations and Trigger Characteristics

Trigger ID[a]	GRB Name	Trigger Time (UTC)	Search Method[b]	Gain Mode	R.A. (deg)	Decl. (deg)	err (deg)	Location Source[c]	Kinds of GRB Samples[d]
HEB170626040	GRB 170626B	2020-07-16T07:34:29.50	BLIND	NG	289.8	−19.2	5.0	IPN	S
HEB170626400	GRB 170626A	2017-06-26T09:37:22.32	BLIND	NG	165.4	56.5	1.0	Fermi/GBM	G
HEB170705115	GRB 170705A	2017-07-05T02:45:59.00	BLIND	NG	191.7	18.3	0.1	Swift	G
HEB170708045	GRB 170708A	2017-07-08T01:06:11.25	BLIND	LG	335.8	19.8	4.6	IPN	S
HEB170712139	GRB 170712A	2017-07-12T03:20:30.00	BLIND	LG	…	…	…	…	B
HEB170714049	GRB 170714B	2017-07-14T01:10:51.10	BLIND	NG	18.2	29.5	…	Fermi/GBM	G
HEB170718152	…	2017-07-18T03:39:30.00	TARGETED	NG	102.3	−35.0	…	Fermi/GBM	G
HEB170726248	GRB 170726B	2017-07-26T05:58:15.42	BLIND	NG	166.4	−34.0	2.8	Fermi/GBM	G
HEB170726793	GRB 170726A	2017-07-26T19:02:59.51	BLIND	NG	297.8	6.6	…	Fermi/GBM	G
HEB170728960	GRB 170728B	2017-07-28T23:03:19.00	BLIND	NG	238.0	70.1	…	Fermi/GBM	G

Notes.
[a] The trigger ID starts with a "HEB" label, which means "HE-detected burst".
[b] As clarified in Section 3, BLIND means blind search, and TARGETED means targeted search.
[c] The uncertainties of the locations from Swift/BAT are 90% containment, including the systematic uncertainty, while those from Fermi/GBM and other detections are 1σ containment, statistical only. If the location source is from interplanetary network (IPN) triangulation, the error is determined to be the maximum dimension of the error box area. Instrument detections are defined as Fermi/LAT: Large Area Telescope, and IBIS: Imager on Board of the Integral Satellite in INTEGRAL.
[d] As shown in Table 2, G means GOLDEN, S means SILVER, and B means BRONZE, I: IRON.

(This table is available in its entirety in machine-readable form.)

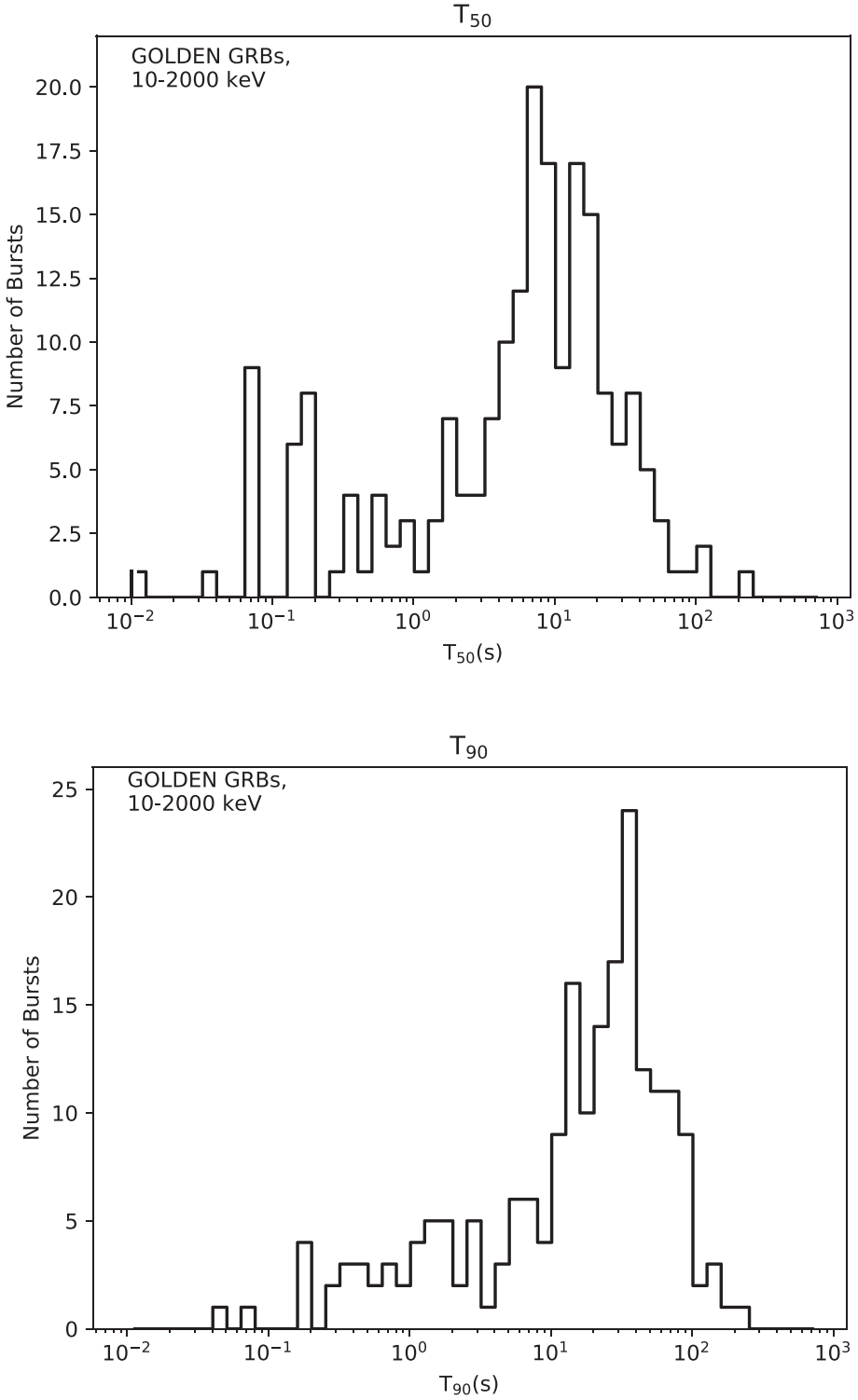

Figure 10. Distribution of "GOLDEN" GRB durations in the 10–2000 keV energy range. The upper plot shows T_{50}, and the lower plot shows T_{90}.

6. Discussion and Summary

Histograms of the T_{50} and T_{90} distributions are shown in the 10–2000 keV energy range in Figure 10. Using the conventional division between short and long GRB classes ($T_{90} = 2$ s), we find 35 (17%) of the 202 "GOLDEN" GRBs to be in the short regime. Within the quoted duration errors, the number of short GRB events ranges from 28 (14%) to 39 (19%). This is consistent with the results from the Fermi/GBM GRB catalog, covering 10 years (von Kienlin et al. 2020), which has 395 (17%) short GRBs from statistics in 10–1000 keV. Due to the limited statistics of GRB numbers, we do not perform lognormal fits to the distribution of the durations.

Figure 11 shows the comparison of durations (T_{90}) from joint analyses with other missions and those from HXMT/CsI GRB data, where the red line denotes the case when these two are equivalent to each other. Most GRBs are below the red line

Table 4
Durations (10–2000 keV) from Joint Analyses with "GOLDEN" GRB Samples

Trigger ID	Detectors Used	T_{50} (s)	T_{50} Start (s)	T_{90} (s)	T_{90} Start (s)	T_{90} Only with HXMT/Cs I Counts (s)
HEB170626400	HXMT/CsI, Fermi-GBM (n0, n1, n2, b0)	7.040 ± 0.264	1.248	12.416 ± 0.202	0.224	12.690 ± 0.081
HEB170705115	HXMT/CsI, Fermi-GBM (n8, nb, b1)	33.792 ± 3.714	0.496	68.672 ± 1.601	−6.416	18.460 ± 6.340
HEB170714049	HXMT/CsI, Fermi-GBM (n3, n7, b0, b1)	0.128 ± 0.064	−0.156	0.448 ± 0.143	−0.412	0.835 ± 0.220
HEB170718152	HXMT/CsI, Fermi-GBM (n3, n4, b0)	10.624 ± 1.943	−7.144	24.768 ± 3.562	−13.352	24.160 ± 3.322
HEB170726248	HXMT/CsI, Fermi-GBM (n9, n7)	1.344 ± 0.143	−0.232	5.824 ± 1.537	−1.704	2.580 ± 0.061
HEB170726793	HXMT/CsI, Fermi-GBM (n8, n7, b1)	10.432 ± 0.272	1.364	26.240 ± 2.689	−5.612	22.871 ± 0.901
HEB170728960	HXMT/CsI, Fermi-GBM (n6, n9, b1)	12.864 ± 0.202	0.684	19.840 ± 0.962	0.364	16.860 ± 2.371
HEB170731751	HXMT/CsI, Fermi-GBM (n0, n3, b0)	41.664 ± 1.604	4.336	59.584 ± 3.623	−2.768	28.141 ± 6.360
HEB170802637	HXMT/CsI, Fermi-GBM (n6, n8, b1)	0.192 ± 0.091	0.696	2.176 ± 1.793	−1.288	0.820 ± 0.014
HEB170817908	HXMT/CsI, Fermi-GBM (n0, n1, n2, n5, b0)	1.472 ± 0.143	0.544	2.688 ± 0.202	0.288	2.620 ± 0.081

(This table is available in its entirety in machine-readable form.)

Table 5
Durations (40–800 keV for NG Mode, 200–3000 keV for LG Mode) of "SILVER" and "BRONZE" GRB Samples

Trigger ID	Detectors Used	T_{50} (s)	T_{50} Start (s)	T_{90} (s)	T_{90} Start (s)
HEB170626040	HXMT/CsI	2.504 ± 0.707	3.840	6.511 ± 1.120	1.836
HEB170708045	HXMT/CsI	0.050 ± 0.014	−0.004	0.200 ± 0.022	−0.034
HEB170712139	HXMT/CsI	3.504 ± 0.708	−2.628	8.511 ± 1.119	−5.631
HEB170801208	HXMT/CsI	0.020 ± 0.014	0.009	0.460 ± 0.750	−0.421
HEB170803917	HXMT/CsI	0.160 ± 0.014	0.837	0.260 ± 0.014	0.787
HEB170805596	HXMT/CsI	0.040 ± 0.032	0.192	0.270 ± 0.487	−0.028
HEB170805610	HXMT/CsI	0.300 ± 0.141	0.476	2.000 ± 0.141	−1.024
HEB170829270	HXMT/CsI	2.002 ± 0.707	0.374	5.507 ± 2.696	−0.627
HEB170901499	HXMT/CsI	8.020 ± 2.832	3.274	46.118 ± 28.143	−0.736
HEB170904406	HXMT/CsI	5.901 ± 0.224	2.475	11.403 ± 0.608	0.175

(This table is available in its entirety in machine-readable form.)

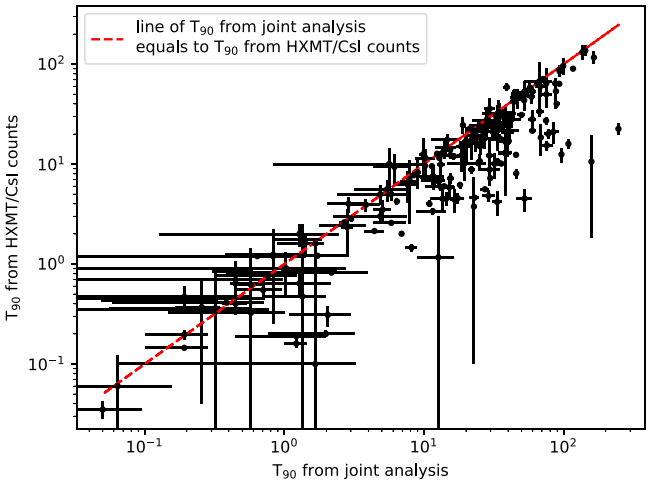

Figure 11. Comparison between the durations (T_{90}) of "GOLDEN" GRBs from a joint analysis and those obtained from HXMT/Cs I GRB counts. The red line denotes the case when these two are equal to each other.

because the energy range of HXMT/CsI is higher than the ranges of other missions, such as Fermi/GBM, and because GRBs tend to be shorter at higher energy. Therefore, a joint analysis is necessary for the measurement of the duration in 10–2000 keV.

Despite the limited statistics of "GOLDEN" GRBs, as shown in Figure 12, the anticorrelation of spectral hardness with duration is confirmed by the relation between the hardness and duration, where the hardness is calculated as the ratio of the flux density from spectral parameters determined from time-averaged spectral fits in 50–300 keV to that in 10–50 keV. We note that here the durations are those from joint analyses in the energy range of 10–2000 keV, which also illustrates the anticorrelation between the hardness of GRB spectra and duration.

Peak fluxes on timescales of 64 ms, 256 ms, and 1024 ms are shown in Figures 13, 14, and 15, respectively. Distributions of GRB fluence are shown in Figure 16. These distributions are not consistent with those from von Kienlin et al. (2020). The contributions are very small both below

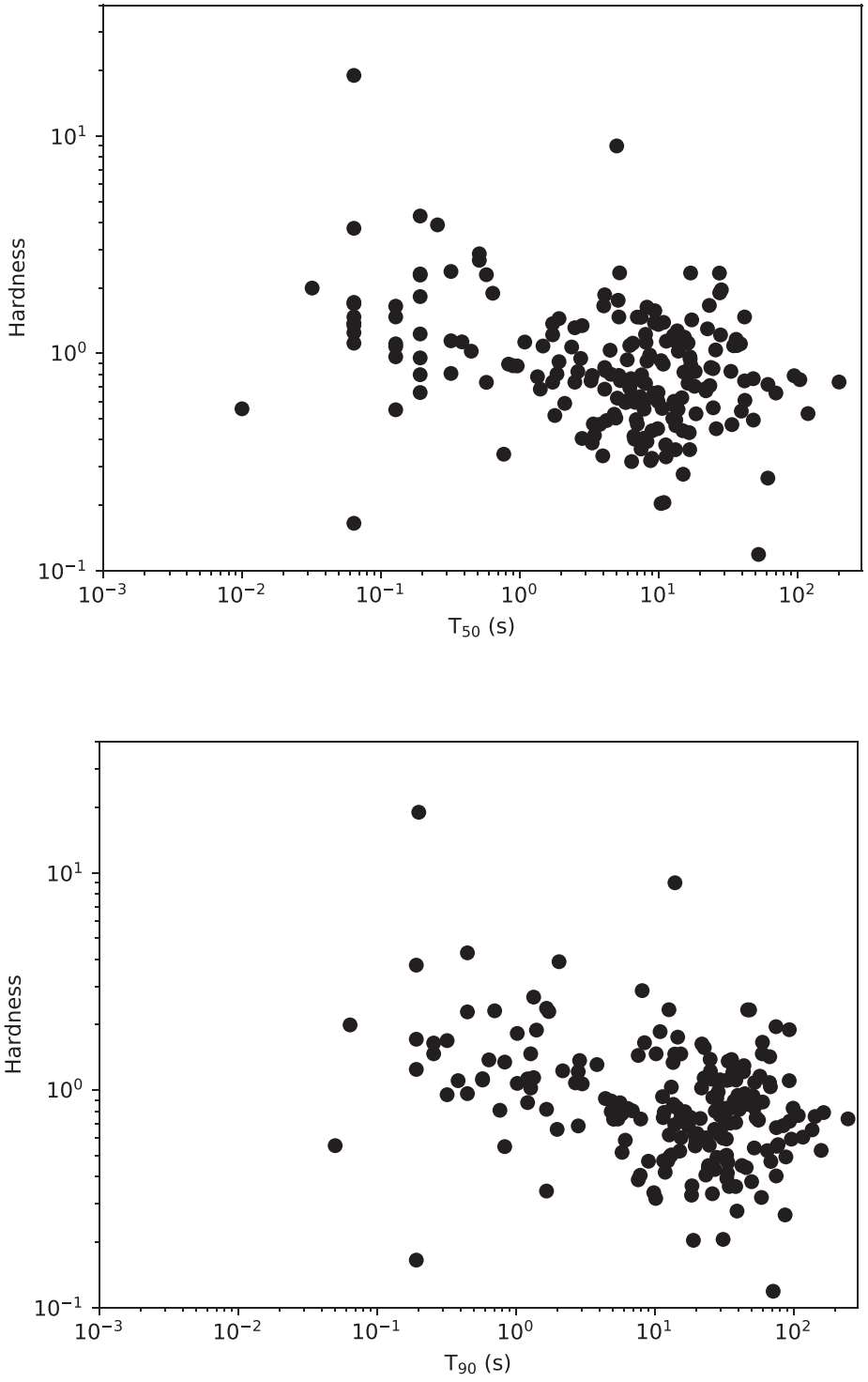

Figure 12. Scatter plots of spectral hardness vs. duration for the two duration measures T_{50} (upper plot) and T_{90} (lower plot) as shown in Figure 10. The hardness is calculated as the ratio of the flux density from spectral parameters determined from time-averaged spectral fits in 50-300 keV to that in 10–50 keV. For clarity, the estimated errors are not shown, but they can be quite large for the weak events. Nevertheless, the anticorrelation of spectral hardness with burst duration is evident.

10^{-7} erg cm^{-2} and 1 ph cm^{-2} s^{-1} in the distributions of fluence and peak fluxes. This could be explained by the sharp fall of the effective area below 100 keV. Weak short GRBs cannot cause enough statistics in HXMT/CsI, and thus cannot be detected significantly. Extremely bright GRBs would not be included in "GOLDEN" samples because they are very likely to cause data saturation in HXMT and are included in the "IRON" samples.

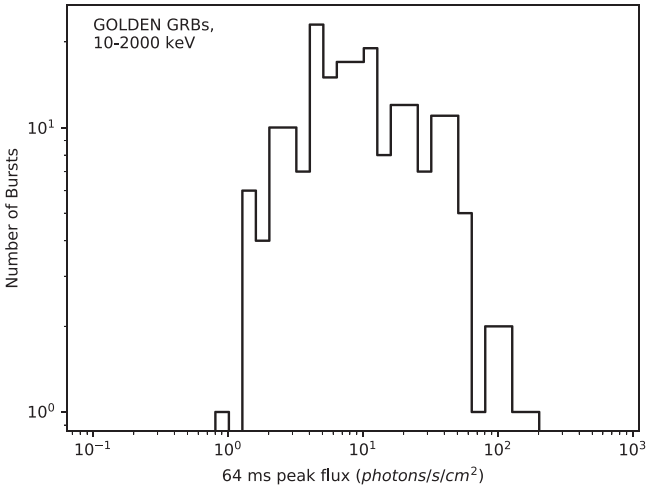

Figure 13. Distribution of the "GOLDEN" GRB peak flux on the 0.064 s timescale in the energy range of 10–2000 keV.

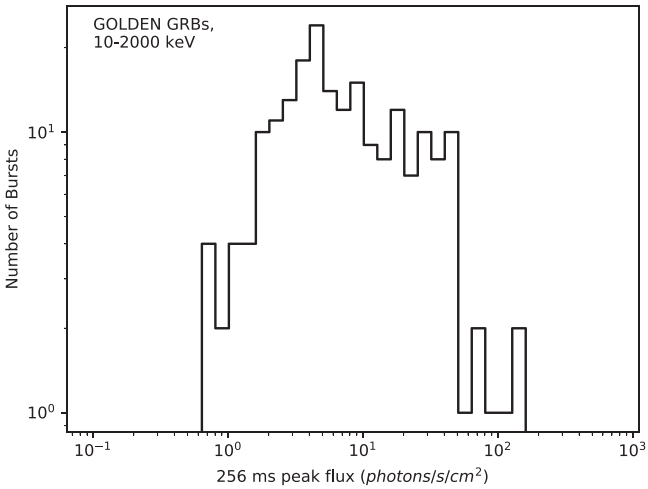

Figure 14. Distribution of the "GOLDEN" GRB peak flux on the 0.256 s timescale in the energy range of 10–2000 keV.

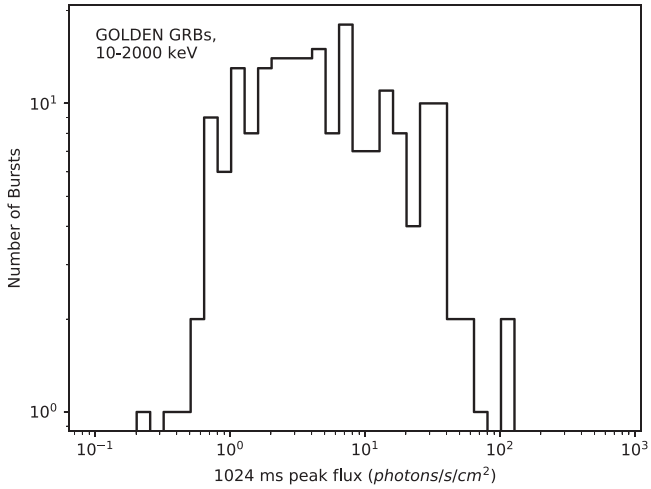

Figure 15. Distribution of the "GOLDEN" GRB peak flux on the 1.024 s timescale in the energy range of 10–2000 keV.

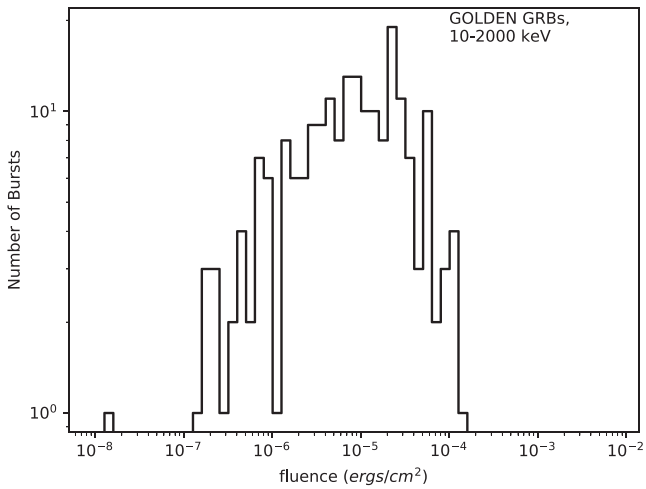

Figure 16. Distribution of the "GOLDEN" GRB fluence in the energy range of 10–2000 keV.

Table 6
Fluence and Peak Flux (10–2000 keV) from Joint Analyses with "GOLDEN" GRB Samples

Trigger ID	Fluence (erg cm^{-2})	PF64 (ph cm^{-2} s^{-1})	PF256 (ph cm^{-2} s^{-1})	PF1024 (ph cm^{-2} s^{-1})
HEB170626400	1.54e-05 ± 1.43e-07	41.78 ± 3.65	38.89 ± 1.64	32.66 ± 0.68
HEB170705115	2.03e-05 ± 6.04e-07	40.64 ± 7.53	32.12 ± 3.08	21.31 ± 1.22
HEB170714049	2.31e-07 ± 2.72e-08	6.08 ± 1.26	2.52 ± 0.38	0.85 ± 0.11
HEB170718152	2.29e-06 ± 5.94e-08	3.50 ± 0.75	2.21 ± 0.31	1.57 ± 0.12
HEB170726248	1.50e-06 ± 1.01e-07	4.55 ± 0.92	3.07 ± 0.43	2.19 ± 0.18
HEB170726793	8.23e-06 ± 1.08e-07	11.03 ± 1.07	7.71 ± 0.43	3.79 ± 0.16
HEB170728960	4.36e-06 ± 9.99e-08	24.14 ± 2.25	21.56 ± 1.09	11.19 ± 0.38
HEB170731751	3.07e-06 ± 9.91e-07	1.89 ± 0.51	1.10 ± 0.21	0.75 ± 0.08
HEB170802637	3.13e-06 ± 1.78e-07	36.30 ± 3.41	26.20 ± 1.38	8.57 ± 0.39
HEB170817908	5.50e-06 ± 9.30e-08	14.55 ± 0.86	10.09 ± 0.42	6.79 ± 0.17

(This table is available in its entirety in machine-readable form.)

This work made use of the data from the Insight-HXMT mission, a project funded by the China National Space Administration (CNSA) and the Chinese Academy of Sciences (CAS). The authors acknowledge support from the National Program on Key Research and Development Project (grant Nos. 2016YFA0400801, 2021YFA0718500), the National Natural Science Foundation of China under grant No. U1838113, and the Strategic Priority Research Program on Space Science, the Chinese Academy of Sciences (grant Nos. XDB23040400, XDA15052700). The authors are very grateful for the public data of Fermi/GBM, Swift/BAT, and GECAM.

Appendix
Light Curves and Spectra of GRB 200125B, GRB 210121A and GRB 210112A

The light curve, spectra, photon flux light curve, and duration of GRB 200125B are shown in Figures 17–20. The spectra and fitted results of GRB 210121A and GRB 210112A are shown in Figures 21 and 22.

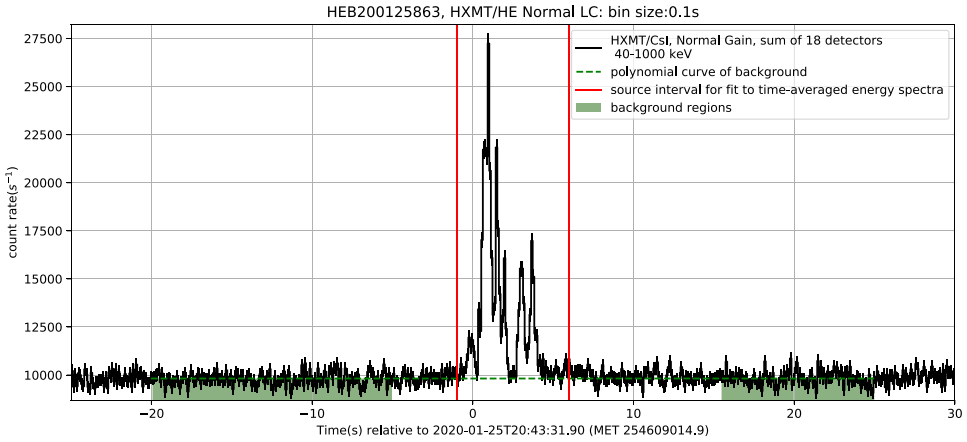

Figure 17. Light curve of GRB 200125B (HEB200125863) from 18 CsI detectors. Vertical lines indicate the regions selected for the fit to the time-averaged spectra. Green regions define the background region. Here MET means the mission-elapsed time of HXMT.

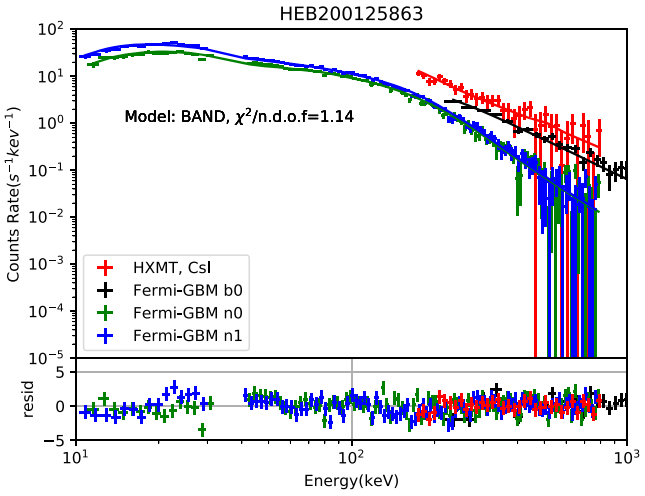

Figure 18. Joint analysis of the time-averaged spectrum of GRB 200125B (HEB200125863). Data from 18 HXMT/CsI detectors and from Fermi/GBM NaI detectors 0 and 1, and from the BGO detector 0 are used.

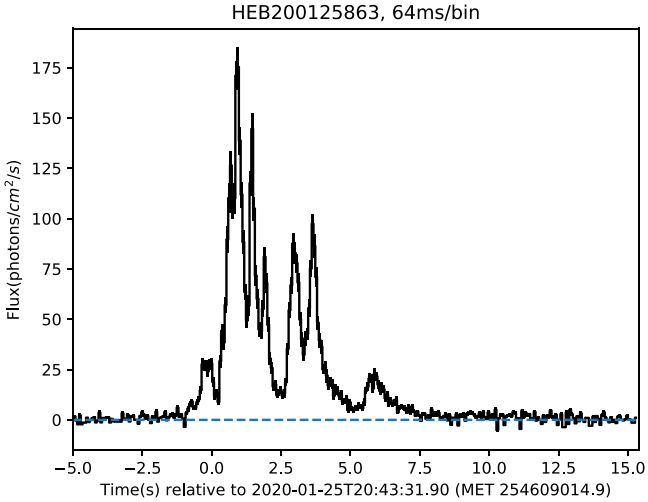

Figure 19. Photon flux light curve for GRB 200125B (HEB200125863) produced by the duration analysis. Data from 18 HE/CsI detectors and from Fermi/GBM NaI detector 0 and 1, and from the BGO detector 0 are used. Here MET means the mission-elapsed time of HXMT.

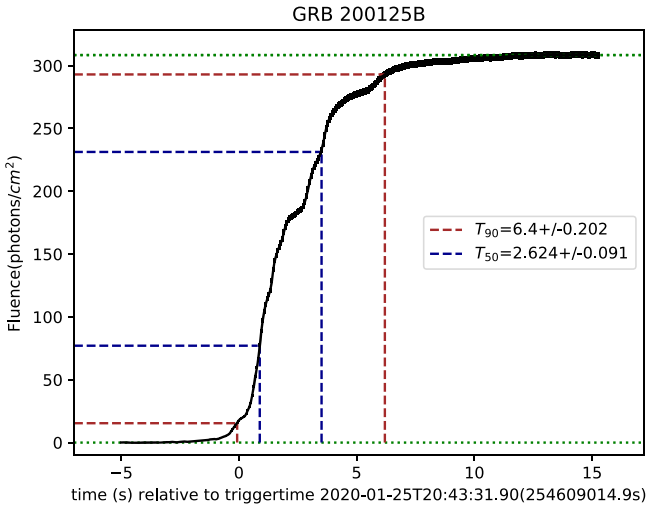

Figure 20. The duration plot for GRB 200125B (HEB200125863). Horizontal dashed lines in dark red are drawn at 5% and 95% of the total fluence, while those in dark blue are at 25% and 75%. Vertical dotted lines are drawn at the times corresponding to these same fluences, thereby defining the T_{50} and T_{90} intervals. The dotted green horizontal lines correspond to 0% and 100% of the total integration of the flux. Here MET means the mission-elapsed time of HXMT.

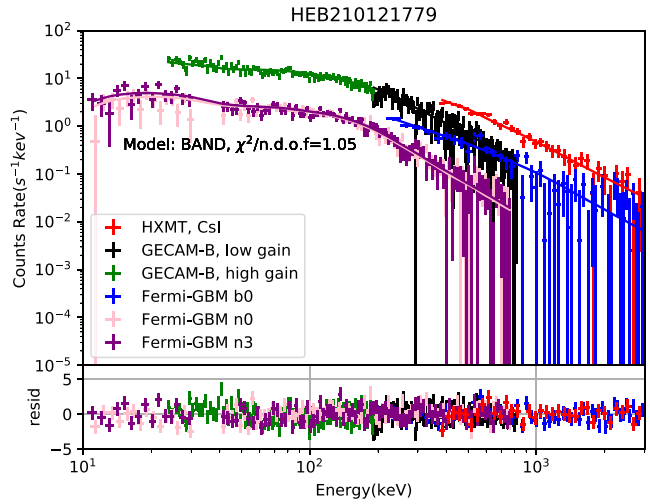

Figure 21. Joint analysis of the time-averaged spectrum of GRB 210121A (HEB210121779). Data from 18 HE/CsI detectors and from the Fermi/GBM NaI detector 0 and 3, and from the BGO detector 0 are used.

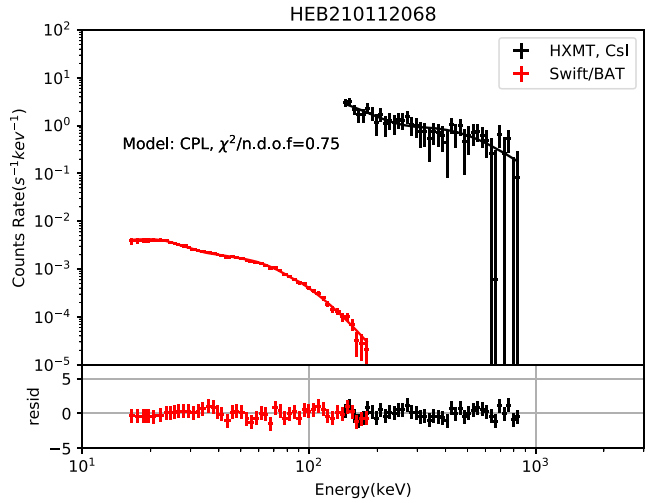

Figure 22. Joint analysis of the time-averaged spectrum of GRB 210112A (HEB210112068). Data from 18 HE/CsI detectors and from Swift/BAT are used.

ORCID iDs

Xin-Ying Song https://orcid.org/0000-0002-2176-8778
Shao-Lin Xiong https://orcid.org/0000-0002-4771-7653
Shuang-Nan Zhang https://orcid.org/0000-0001-5586-1017
Cheng-Kui Li https://orcid.org/0000-0001-5798-4491
Xiao-Bo Li https://orcid.org/0000-0003-4585-589X
Xu-Fang Li https://orcid.org/0000-0002-2793-9857
Gang Li https://orcid.org/0000-0001-5067-1599
Jin-Yuan Liao https://orcid.org/0000-0001-8277-6133
Qi Luo https://orcid.org/0000-0003-1853-7810
Shuo Xiao https://orcid.org/0000-0003-2957-2806
Deng-Ke Zhou https://orcid.org/0000-0002-7420-9988
Fang-Jun Lu https://orcid.org/0000-0003-3248-6087
Li-Ming Song https://orcid.org/0000-0003-0274-3396
Ming-Yu Ge https://orcid.org/0000-0002-2749-6638
Shu-Mei Jia https://orcid.org/0000-0002-5203-8321
Bing Li https://orcid.org/0000-0002-0238-834X

References

Agostinelli, S., Allison, J., Amako, K., et al. 2003, NIMPA, 506, 250
Band, D., Matteson, J., Ford, L., et al. 1993, ApJ, 413, 281
Blackburn, L., Briggs, M. S., Camp, J., et al. 2015, ApJS, 217, 8
Cai, C., Xiong, S. L., Li, C. K., et al. 2021, MNRAS, 508, 3910

Cao, X. L., Jiang, W. C., Meng, B., Zhang, W. C., & Luo, T. 2020, SCPMA, 63, 249504
Cash, W. 1979, ApJ, 228, 939
Chen, Y., Cui, W. W., Li, W., et al. 2020, SCPMA, 63, 249505
Goldstein, A., Burgess, J. M., Preece, R. D., et al. 2012, ApJS, 199, 19
Goldstein, A., Burns, E., Hamburg, R., et al. 2016, arXiv:1612.02395
Goldstein, A., Hamburg, R., Wood, J., et al. 2019, arXiv:1903.12597
Guidorzi, C., Orlandini, M., Frontera, F., et al. 2020, A&A, 642, A160
Hurley, K., Briggs, M. S., Kippen, R. M., et al. 1999, ApJS, 120, 399
Ishida, M., Tsujimoto, M., Kohmura, T., et al. 2014, PASJ, 63, S657
Kocevski, D., Burns, E., Goldstein, A., et al. 2018, ApJ, 862, 152
Koshut, T. M., Paciesas, W. S., Kouveliotou, C., et al. 1996, ApJ, 463, 570
Li, T. P., Xiong, S. L., Zhang, S. N., et al. 2018, SCPMA, 61, 31011
Li, X., Li, X., Tan, Y., et al. 2020, JHEAp, 27, 64
Li, X. F., Liu, C. Z., Chang, Z., et al. 2019, JHEAp, 24, 6
Li, Z. W., Liao, J. Y., Li, C. K., et al. 2017, GCN, 21593, 1
Liu, C. Z., Zhang, Y. F., Li, X. F., et al. 2020, SCPMA, 63, 249503
Luo, Q., Liao, J.-Y., Li, X.-F., et al. 2020, JHEAp, 27, 1
Preece, R. D., Briggs, M. S., Mallozzi, R. S., et al. 1998, ApJL, 506, L23
Sakamoto, T., Pal'Shin, V., Yamaoka, K., et al. 2011, PASJ, 63, 215
Tierney, D. 2011, in Proc. Science 115, 8th Integral Workshop: The Restless Gamma-ray Universe (INTEGRAL 2010) (Trieste: Sissa), 103
Tsujimoto, M., Guainazzi, M., Plucinsky, P. P., et al. 2011, A&A, 525, A25
von Kienlin, A., Meegan, C. A., Paciesas, W. S., et al. 2020, ApJ, 893, 46
Xiao, S., Xiong, S., Liu, C., et al. 2020, JHEAp, 26, 58
Xie, F., Zhang, J., Song, L. M., Xiong, S. L., & Guan, J. 2015, Ap&SS, 360, 1
Zhang, P., Wang, W., Su, Y., et al. 2021, ApJ, 918, 42
Zhang, S., Zhang, S. N., Lu, F. J., et al. 2018, Proc. SPIE, 10699, 434
Zhang, S. N., Li, T. P., Lu, F. J., et al. 2020, SCPMA, 63, 249502
Zheng, Y. G., Cai, C., Du, Y. F., et al. 2020, GCN, 26815, 1